Calcium imaging in freely-moving mice during electrical stimulation of deep brain structures

J. K. Trevathan*, A. J. Asp, E. N. Nicolai, J. M. Trevathan, N.A. Kremer, T.D. Kozai, D. Cheng, M. Schachter, J. J. Nassi, S. L. Otte, J. G. Parker, J. L. Lujan*, K. A. Ludwig*

Abstract

Over decades of study in humans and animal models, our understanding of mechanisms by which electrical stimulation interacts with neuronal and non-neuronal elements – e.g. neuropil, cell bodies, glial cells, etc. – has steadily improved. However, there remains a lack of consensus regarding how electrical stimulation leads to the therapeutic effects during deep brain stimulation (DBS) and other neuromodulation therapies. This discord stems in part from technical limitations of commonly used non-invasive imaging and invasive electrophysiological techniques, namely, the inability to perform stable recordings of activity from many neuronal and non-neuronal cells with high spatial and temporal resolution in freely-moving animals. Single-photon, head-mounted, miniature microscopy of neurons expressing the genetically encoded calcium sensor GCaMP overcomes many of these limitations, providing a unique opportunity for studying the mechanisms of neuromodulation therapies during pathological behaviors in relevant disease models.

Herein, we describe a novel experimental paradigm combining subthalamic nucleus (STN) electrical stimulation with single-photon calcium imaging of the dorsal striatum via a head-mounted miniature microscope in healthy and 6-hydroxydopamine lesioned parkinsonian mice during minimally constrained behavior. We demonstrate the capabilities of this technique for measuring stimulation-evoked changes in neural activity and describe the challenges associated with surgical procedures, behavioral evaluation, and data analysis. Data collected using this methodology suggest that neuromodulation produces behavior dependent cellular responses and that individual striatal cells respond differently under the same electrical stimulation paradigm. These findings stress the need for a framework that allows for the study of neuromodulation techniques such as DBS during relevant pathological behavior.

Introduction

A multitude of neurologic and psychiatric disorders affect up to one billion people worldwide[1] and can originate from genetic or congenital abnormalities, infections, neural injury, malnutrition, environmental issues, lifestyle choices, or idiopathic causes that may result in pathological brain structure and neural activity. Up to thirty percent of the patients diagnosed with brain disorders can remain refractory to conventional pharmacologic, behavioral, and surgical interventions[2,3]. To address this patient population, the last 30 years have seen a significant expansion in the application of devices to electrically stimulate the nervous system for therapeutic effect, known as neuromodulation therapies, that have become established forms of treatment for patients suffering from these severe and intractable neurologic and psychiatric conditions. For example, electrical stimulation of deep brain structures, known as deep brain stimulation (DBS), has received approval from the United States Food and Drug Administration (FDA) for the treatment of advanced PD, tremor[4–6], and epilepsy[7–10]. Additionally, humanitarian device exemptions have been granted for treatment of dystonia and obsessive-compulsive disorder[6].

Neuromodulation treatment involves electrical stimulation of anatomical targets that are associated with pathological patterns of neural activity specific to a given disorder[11]. Although the electrical stimulation is local to the electrode, both clinical and preclinical studies have demonstrated that the efficacy of these techniques is associated with changes in the wider neural network as well as local changes in neural activity[12,13]. Stimulation-evoked neural network changes have been found for a variety of targets. For example, DBS of the subthalamic nucleus (STN) for PD has been associated with increased electrophysiological activity in neurons within the globus pallidus[14–16] and substantia nigra[17–19]. Stimulation of the ventral capsule/ventral striatum and cingulate cortex for major depressive disorder (MDD) has been found to affect neural activity in the anterior insula as well as the prefrontal, premotor, and dorsal anterior cingulate cortices[20,21]. DBS of the thalamic ventral intermedius (VIM) nucleus for tremor has been shown to change neural activation across the cerebello-thalamo-cortical circuit[22,23]. This alteration is associated with reduction of pathologic oscillations in cortical, thalamic, and cerebellar nuclei, leading to tremor reduction in patients with essential tremor[24,25].

Studies to elucidate the mechanisms of action of DBS have centered on measuring the physiological responses evoked by DBS using non-invasive functional imaging[21,26–28] and electrophysiological recording techniques[14–19]. Unfortunately, these techniques have inherent limitations that make it difficult to parse out the multimodal mechanisms by which DBS may alter the activity of a neural circuit during the execution of complex behavior. Functional imaging techniques such as functional magnetic resonance imaging (fMRI) and positron emitted tomography (PET) have low spatial (in the order of a millimeter) and temporal resolution (in the order of several seconds) and can only be performed during simple behavioral paradigms that restrict overall movement[29,30]. Electrophysiological recordings from single-units or multi-unit populations provide high spatial and temporal resolution but are limited to sparse sampling (typically under 100 electrode contacts separated by hundreds of microns), provide limited or unreliable information about recorded cell-types and their exact spatial locations[31], and have a have low signal stability over time that limits the study of DBS induced plastic changes in circuit function[32,33]. As DBS induces electromagnetic cross-talk and disturbs the recording electrode/electrolyte interface, electrical stimulation also generates spurious artifacts that can resemble electrophysiological responses[34,35].

The intended therapeutic and unintended effects of DBS are likely mediated through multiple mechanisms driven by multiple cell-types that alter the function of a neural circuit. The relative contribution of each mechanism may evolve over the course of stimulation as a function of stimulation induced changes in the electrode/tissue interface[36,37], stimulation induced plasticity in neuronal and non-neuronal cells near the electrode[38], stimulation induced post-synaptic plasticity[39], changes in behavior state[40], and adjunct drug status[41]. Clinical use of
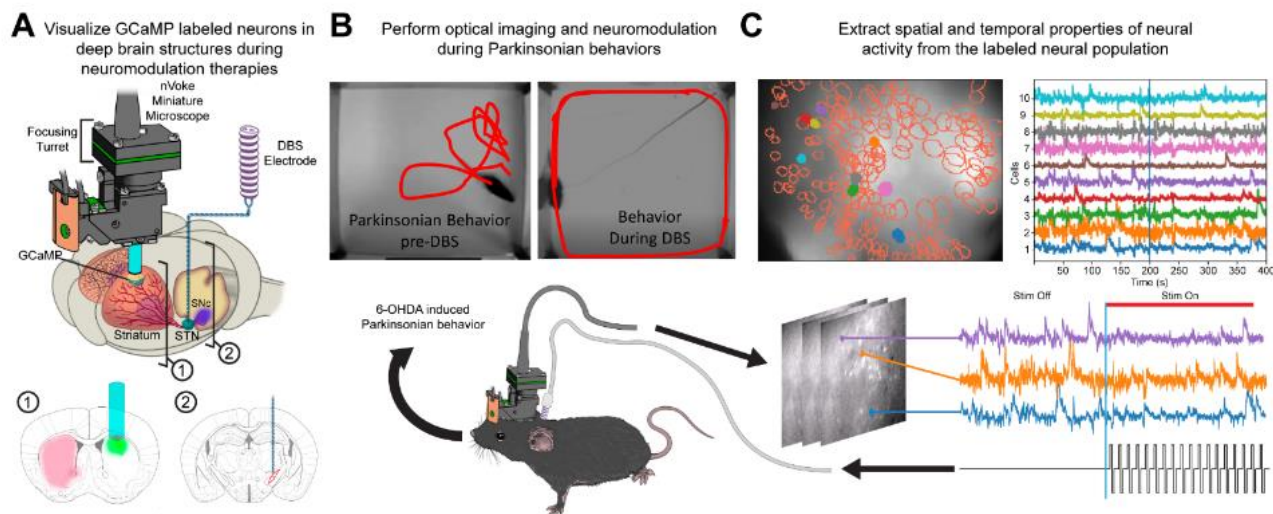
2

Figure 1. Experimental objectives. A) Visualization of GCaMP labeled neurons in deep brain structures of 6-hydroxy dopamine (6-OHDA) lesioned mice was performed with a miniature head-mounted microscope (Inscopix, Inc., Palo Alto, CA). The substantia nigra pars compacta (SNc) was lesioned via an injection of 6-hydroxydopamine (6-OHDA) to create an animal model of Parkinson's disease (PD). Calcium imaging of cells labeled with GCaMP, a genetically encoded calcium indicator commonly used to detect neural activity, was performed through a gradient index (GRIN) lens implanted into the striatum (1). Additionally, a twisted bipolar electrode was inserted into the subthalamic nucleus (STN) to deliver deep brain stimulation (DBS) (2). **B)** Optical imaging and electrical stimulation of the STN were performed during open field behavior while position of the animal was tracked (red lines) to assess behavioral changes. **C)** Spatial (outlines) and temporal (traces) properties of neural activity, shown on top left and right panels, respectively, were extracted from the recorded miniature microscopy videos and analyzed to determine changes in striatal activity that occurred during stimulation (bottom panel).

neuromodulation therapies in diverse conditions such as epilepsy, depression and Tourette's syndrome consistently demonstrate significant improvement in patient outcomes with slow onsets over periods of several weeks to several months[21,42–50]. Whether these slow therapeutic responses are a result of placebo effects, changes to tissue local to the implant, wider network adaptation, or combinations of all the above, remains unknown. Consequently, experimental paradigms for elucidating the therapeutic mechanisms of DBS ideally need to be able to record from stable populations of hundreds of genetically specified cells with high spatial and temporal resolution across timeframes of weeks to months. These measurements need to be made during behaviors relevant to the clinical indication being studied to understand the role of both the local, circuit, and systems level dependencies in the neural response to DBS.

Here we describe a novel experimental paradigm combining electrical stimulation of the STN with chronic single-photon calcium imaging of striatal activity in behaving mice via a head-mounted miniature microscope (Figure 1A,B). We characterize the downstream cellular response to electrical stimulation across hundreds of spatially identifiable cells located within the striatum of the well-studied 6-hydroxydopamine (6-OHDA) mouse model of Parkinson's Disease (Figure 1C). We demonstrate how synchronous neural activity evoked by electrical stimulation confound some state-of-the-art miniature microscopy analysis techniques and demonstrate the utility of constrained non-negative matrix factorization (CNMF-E) in addressing these issues. Finally, we describe differences in striatal neural activity during STN stimulation between freely-moving and anesthetized states. We also demonstrate that cells within striatum in close proximity frequently exhibit very different responses to the same STN stimulation pattern. These results underscore the utility of head-mounted miniature microscopy for studying

3

DBS and other neuromodulation techniques and provide a framework to expand this experimental paradigm to the study of DBS mechanisms for other clinical indications.

Methods

The experimental protocol requires the successful implantation of four separate components: 1) induction of calcium indicator, GCaMP6m, expression via a unilateral injection of an AAV9 viral vector into striatum (Figure 2A,B), 2) placement of a Gradient Refractive Index (GRIN) lens in the target recording location just above striatum (Figure 2A,C), 3) induction of a Parkinsonian phenotype via unilateral injection of 6-OHDA into the substantia nigra pars compacta (SNc) (Figure 2A,B), and 4) placement of a bipolar stimulating electrode within the STN for application of electrical stimulation (Figure 2A,B).

Subjects

In total 30 adult C57BL/6J male mice approximately 25-30g (Jackson Laboratories, Bar Harbor, ME) were for verifying 6-OHDA lesioning and behavior (n=15), chronic recordings in healthy mice (n=5) and parkinsonian mice (n=10). Of the ten parkinsonian mice, six were removed from analysis due to surgical complications and lost headcaps while the others were used for data collection while under anesthesia (n=4). Two of the four animals used for the anesthetized studies were used for the awake calcium imaging studies.

Animals were group-housed and maintained under a standard light/dark cycle with ad libitum access to food and water. All experimental procedures were approved by the Institutional Animal Care and Use Committee (IACUC) and carried out in accordance with the U.S. National Research Council Guide for the Care and Use of Laboratory Animals.

Injection of Viral Vector and Dopaminergic Lesioning

Mice were anesthetized in an induction chamber with 5% isoflurane (inhalation) and then maintained with a continuous flow of 1-2% isoflurane-oxygen mixture during stereotactic surgery (Kopf Systems, Tujunga, CA). A midline incision was performed to expose the skull and burr holes were made above the dorsal striatum (ML=1.65, AP=1.0 from bregma) and substantia nigra pars compacta (SNc) (ML=1.25, AP=–3.5 from bregma), respectively. A Hamilton syringe (Hamilton Company, Reno, NV) controlled by a stereotactically mounted microdrive (WorldPrecision Instruments) was lowered into right dorsal striatum (AP= +1.0 mm, ML=+1.65 mm, DV= -2.7 mm from dura) at an approximate rate of 10µm/sec and used to inject 500 nL of AAV9.CAG.GCaMP6m.WPRE.bGHpA (titer = 5.5E12 GC/mL) at a rate of 100 nL/min (Figure 2B). Brain tissue was given one minute to settle prior to the unilateral AAV injection. The virus was allowed to diffuse for an additional five minutes prior to removing the needle at approximately 10µm/sec.

Immediately following AAV injection, a separate Hamilton syringe was used to inject 6-OHDA (4 mg/kg, i.p.) into the SNc at three depths: DV –4.2, -4, and -3.8 from dura (Figure 2B). Injections of 650 nL at 100 nL/min were delivered. These injections were preceded with a wait period of one minute to allow brain tissue to stabilize prior to each injection, and followed by a wait period of five minutes for diffusion[51]. Insertion, removal and movements of the injection needle were carried out at approximately 10µm/sec. Desipramine HCl was injected (25 mg/kg, i.p.) approximately 30 minutes before the first 6-OHDA injection to prevent uptake of 6-OHDA into monoamine neurons[52]. The burr holes were sealed with Kwik-Sil (World Precision Instruments, Sarasota, FL) before suturing the skin incision. Ketofen (2.5mg/kg, i.p.) and Carpofen (2.5mg/kg, i.p.) were administered to reduce inflammation and provide analgesia. Each animal was allowed to recover individually in a heated home cage until fully mobile and were then returned to social housing.
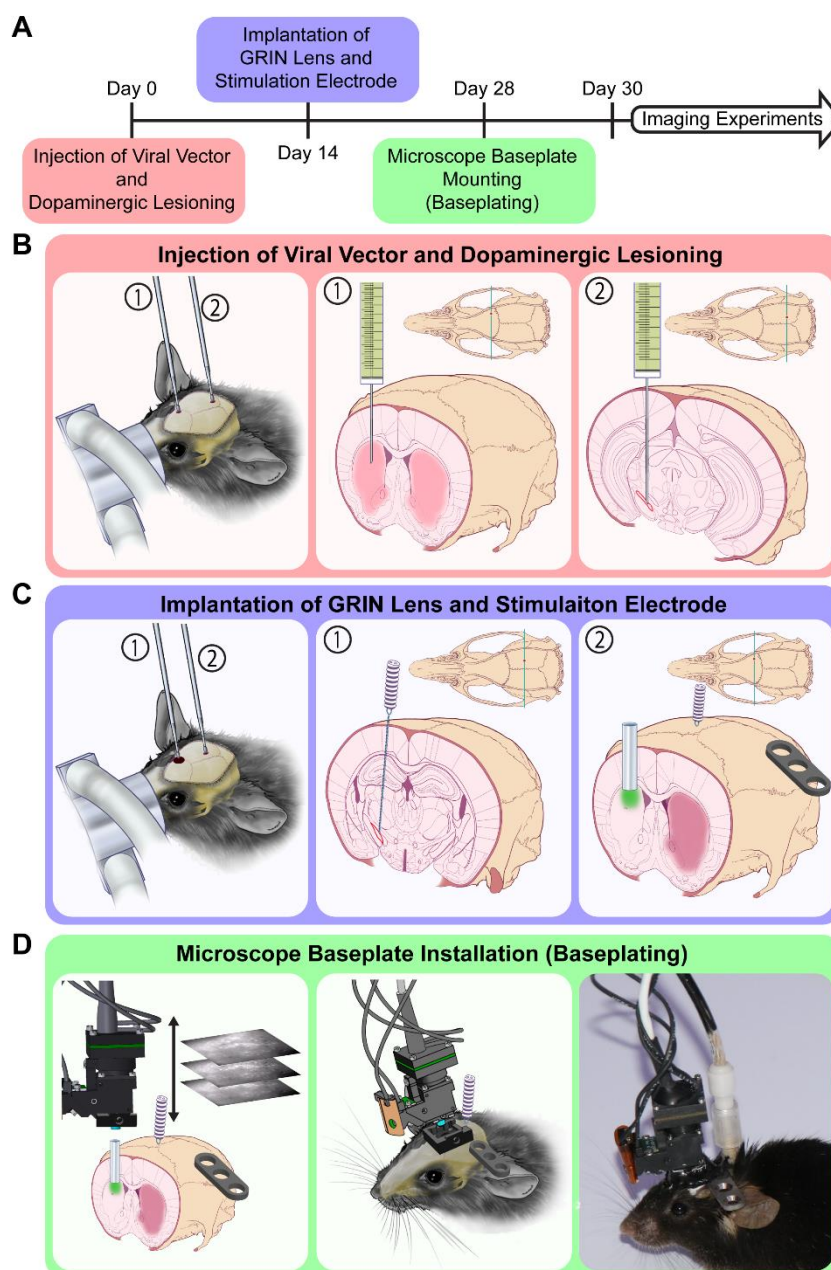
Figure 2. Experimental procedures required for calcium imaging of striatal neural activity during electrical stimulation of the subthalamic nucleus (STN) in awake, freely-behaving Parkinsonian animals. A) Mice underwent staged dopaminergic lesioning, viral transfection, surgical implantation of Graded Index (GRIN) lens and deep brain stimulation (DBS) electrode, and mounting of the microscope baseplate procedures over the course of one month prior to the start of calcium imaging experiments. **B)** At day 0, a unilateral microinjection of AAV9-GCaMP6m was performed into the dorsal striatum under isoflurane anesthesia to induce expression of the GCaMP reporter needed for imaging (1). In the same surgical session, a solution of 6-OHDA was injected ipsilaterally into the substantia nigra pars compacta (SNc) to cause a dopaminergic lesion, thereby resulting in a parkinsonian phenotype (2). **C)** At day 14, a DBS electrode (1) and GRIN lens (2) were implanted into the STN and dorsal striatum, respectively under isofluorane anesthesia. Both implants were secured to the skull via skull screws and dental adhesive. Extra care was placed to avoid covering bregma and the GRIN lens location. The panel on the right shows the baseplate used to mount the microscope. **D)** The microscope, with a baseplate attached, was positioned above the GRIN lens of an awake head-fixed animal positioned on a running wheel (not shown) to encourage movement. The distance from the microscope to GRIN lens was adjusted to optimize the focal plane within the tissue that exhibited the most active and in-focus cell bodies. The microscope baseplate was then affixed to the animal via dental cement and the headcap was coated with black nail polish to prevent contamination from external light sources. The animal was then removed from the head-fixed running wheel and ready for behaving imaging sessions.

Implantation of GRIN Lens and DBS Electrode

Two weeks after injection of viral vector and dopaminergic lesioning animals were prepared for a second surgery as described above. Burr holes were drilled above the dorsal striatum (ML 1.65, AP 1.0 from bregma) and STN (ML 1.45, AP –2.0 from bregma) (Figure 2C). Three bone screws (Component Supply Company, Sparta TN) were placed to add structural support for the C&B Metabond (Parkell, Edgewood, NY) dental cement used to secure the implants. The dura was surgically opened through the STN burr hole using microdissection forceps to allow insertion of the electrode. A twisted bipolar teflon-insulated platinum DBS electrode (Plastics One, Roanoke, VA) with a 500 µm exposed tip and contacts separated to 500 µm apart was inserted to the STN (ML 1.45, AP –2.0, DV -4.7 from dura) at approximately 10 µm/sec (Figure 2C). Through the striatum burr hole, a 1 mm column of tissue above the dorsal surface of the striatum was then aspirated to clear a path for lens implantation while ensuring adequate time for viral transfection[51]. Tissue was aspirated with a blunt 27-gauge needle until white matter of the corpus collosum was visually identified through a Leica M320 surgical microscope (LEICA, Wetzlar, Germany). A small portion of white mater was then carefully to expose the dorsal surface of the striatum for imaging while minimizing tissue damage. A 4 mm long, 1 mm diameter GRIN lens (Inscopix, Palo Alto, CA) was then inserted through the striatal burr hole using a custom-built lens holder to a depth of -2.35 mm from dura (Figure 2C). The custom-built lens holder was fabricated from micropipette tip cut so that ~500µm of the lens was securely held. Kwik-Sil was used to seal both burr holes following implantation of the GRIN lens and DBS electrode. A headbar was mounted so that it extended laterally from the animal's skull contralateral to the implants to allow head-fixing of the animal while installing the microscope baseplate (Figure 2D). C&B Metabond was used to secure the headbar, DBS electrode, and GRIN lens to the skull forming a headcap. The lens surface was protected using a custom-made plastic cap made from the bottom tip of a microcentrifuge tube attached with Kwik-Cast (World Precision Instruments, Sarasota, FL). The same post-operative approach from the previous section was followed.

Microscope Baseplate Installation (Baseplating)

In order to perform calcium imaging during behavior with the nVoke miniature microscope (Inscopix, Palo Alto, CA), a mounting baseplate attached above the GRIN lens is needed. Baseplates were permanently fixed to the headcap of the mouse at the position that maximized the number of active in focus neurons. Due to the locomotion dependence of striatal neural activity[51,53,54], the position was determined by visualizing active neurons in awake head-fixed mice. This procedure was completed two weeks after the GRIN lens implantation to allow for recovery (Figure 2A). Mice were first head-fixed using the previously attached headbar and positioned on a custom-built running wheel to allow locomotion. Locomotion increases striatal neuron activity, making it easier to determine the mounting position that maximizes the number of in focus neurons[51,53]. The microscope focusing turret (Figure 1A) was initially set near the middle of its range to maximize the ability to correct for movement of the baseplate that can occur during dental cement curing. Next, with a baseplate attached, the nVoke microscope was positioned above the surface of the lens (Figure 2D). The microscope was then leveled relative to the surface of the GRIN lens by ensuring the edge of the lens was in focus around the entire circumference. The excitation LED was then turned on to allow visualization of the fluorescent indicator[55]. The dorsoventral position of the miniature microscope was slowly varied over the area of tissue with the largest calcium signal until an imaging plane with in-focus active cells was found (Figure 2D). The mediolateral and anteroposterior positions of the microscope were adjusted as necessary to maximize the number of active cells in the field of view. Once this position was found, the baseplate was attached to the headcap using C&B Metabond. Finally, the headcap was painted with black nail polish to prevent ambient light from filtering through the dental cement and contaminating the recordings (Figure 2D).

Calcium Imaging in Anesthetized Mice

6

To perform calcium imaging in anesthetized mice, the animals were anesthetized with isoflurane, the microscope was attached to the baseplate, and the position of the microscope turret was adjusted to the imaging plane found during the baseplating procedure. This new turret position was recorded and used for all future imaging sessions. A series of 10-second duration, 130 Hz biphasic stimulation trains with 140 us pulse width were applied in one-minute intervals using a Master-8 stimulator with Iso-Flex isolators (A.M.P.I, Jerusalem, Israel). The amplitude of the stimuli was increased until evoked changes in calcium signal were observed. Stimulation trains were then applied at frequencies of 30 Hz, 80 Hz, and 130 Hz and repeated 3 times[40]. These stimulation frequencies were selected based on previous studies in 6-OHDA lesioned rat models showing therapeutic effects at high frequency (80 Hz and 130 Hz) but not low frequency (30Hz) stimulation[40]. Stimulation was triggered and synchronized with optical recordings using the digital I/O from the nVoke microscope system.

Open Field Calcium Imaging During DBS

Mice were placed in a 45 cm by 45 cm open field arena (Med Associates, Fairfax, VT) with the miniature microscope and DBS electrodes connected. Animal movement was recorded with an overhead camera and the nVoke Microscope sync signal provided through the nVoke digital IO box was used trigger to frame acquisition on the overhead camera. In non-lesioned animals without DBS implants, a 30-minute recording was completed two days after mounting the microscope baseplate and was repeated weekly thereafter for four weeks. In 6-OHDA lesioned mice with DBS electrodes implanted a DBS parameter selection session similar to the previously described session under anesthesia was completed four days after mounting the microscope baseplate. During the parameter selection session 1-minute stimulation trains 130 Hz biphasic pulses (140 us) were applied at 3-minute intervals, while simulation amplitude was increased to determine the stimulation threshold for evoking adverse effects. Two 50-minute recordings were then performed on days 6 and 8 after baseplating.

Identification of Neural Signals from Calcium Imaging Data

Calcium imaging data were loaded into Inscopix Data Processing Software (IDPS) (Inscopix, Palo Alto, CA). All data were first spatially down sampled by a factor of two to decrease processing time in subsequent analysis[55,56]. Calcium imaging data sets obtained in awake animals were motion corrected with the Turboreg motion correction algorithm[57] as implemented in IDPS. Cells were identified and their corresponding calcium signals were extracted using three different analysis techniques. These techniques included region of interest (ROI) analysis, principal and independent component analysis (PCA/ICA)[58], and constrained non-negative matrix factorization for microendoscope data (CNMF-E)[59,60]. ROI analysis and PCA/ICA were performed using IDPS. ROI analysis was performed by manually selecting regions in the ΔF/F data that resembled cell body morphology and exhibited changes in relative fluorescence with respect to the surrounding background[61,62]. PCA/ICA was performed using both the default algorithm and parameters from IDPS and a spatiotemporal de-mixing value of 0.1[58]. In this analysis, the number of cells was visually estimated using the same criteria used for ROI analysis; the number of principal components was chosen to be 20% more than the number of cells identified[55,63–65]. We also evaluated the performance of ROI analysis and PCA/ICA after filtering the data with a gaussian spatial bandpass filter with cut-offs selected for each data set based on the size of in-focus cell bodies, ranging from 5 to 13 pixels and 25 to 35 pixels for the low and high frequency cutoffs, respectively. To perform analysis vis CNMF-E, data were downsampled by a factor of 6x and, following motion correction, were exported as TIF files from IDPS and loaded into Matlab® (Natick, MA). To identify neurons via CNMF-E following the recommended procedure from Zhou et al. (2018)[59] and results were computed using Neuroscience Gateway[66]. Briefly, analysis was performed in patch mode using the largest possible patch sizes based on the available memory (128 GB) of the computational node. The ring model of background fluorescence[59] was used for all data sets with neuron and ring sizes selected based

7

on the data set so that ring diameter was approximately 1.5 times the largest neuron diameters and described n Zhou et al. (2018)[59]. Longitudinal alignment of cells between data sets was performed using the Matlab® implementation of the registration algorithm described in Sheintuch et al. 2017[67].

Validation of Neural Signal Identification Techniques on Simulated Data

To compare the performance of different methods for isolating calcium activity given the presence of stimulation induced fluorescence from out of focus neurons, we overlaid the simulated effect of 30 out of focus neurons over real calcium imaging data obtained under anesthesia. The fluorescence of these neurons was spatially distributed according to symmetric 2D gaussians with a standard deviation of 50 pixels centered at random locations within the field of view. The 50-pixel standard deviation was chosen so that the diameter of an out-of-focus neurons was approximately 4 times the diameter of an in-focus neuron. The fluorescence intensity of each neuron was independently simulated according to Vogelstein et al. (2009)[68]. The activity rate of the simulated traces increased during stimulation (Figure S1). Simulated background fluorescence due to out-of-focus neurons was added to real calcium imaging data obtained under anesthesia. Simulated data were used to determine the effectiveness of each analysis technique for identifying cells in the presence of changes in out-of-focus fluorescence during electrical stimulation. ROI analysis, PCA/ICA and CNMF-E were then repeated on data with added simulated background fluorescence contamination and the results compared to uncontaminated data.

Behavioral Evaluation of 6-OHDA Induced Parkinsonian Phenotype

A modified cylinder test was used for the assessment of biased forelimb preference induced by the 6-OHDA lesion[69]. This test is a commonly used method for assessing limb-use asymmetry as a metric for pathologic behavior in 6-OHDA lesioned animals[70–72], Mice were placed in a glass cylinder (15cm wide and 20cm in high) without a prior habituation session and video was recorded 5 min for later scoring by an investigator blinded to treatment group assignments. The number of wall touches (weight bearing paw contact with wall) contralateral and ipsilateral to 6-OHDA lesioned hemisphere were counted during slow-motion playback in VLC media player. These data are presented as a percentage of contralateral touches, calculated as (contralateral touches)/(ipsilateral touches + contralateral touches) × 100.

Perfusion and Tissue Preparation

Just prior to euthanasia with a lethal dose of Euthasol (Virbac AH, Inc., Fort Worth, TX), electrochemical impedance spectroscopy analysis of each stimulation electrode contact was performed using an Autolab PGSTAT302N (Metraohm Autolab, Utrecht, The Netherlands) and following the spectroscopy sweep described in Lempka et al. 2009[73]. Animals with stimulation electrodes exhibiting impedances greater than 120kΩ of impedance at 130Hz were removed from further analysis due to failure of the stimulation electrode. Following euthanasia, transcranial perfusion with 50mL of 0.9% saline, followed by 50mL of 4% paraformaldehyde in 0.1M NaKPO$_4$. Perfused brains were extracted, post-fixed overnight in 4 % paraformaldehyde, and stored in 30% glycerol sinking solution. Cryosectioning with 40 μm slices was performed on a sliding microtome (Leica Biosystems, Wetzlar, Germany). Sections were stored in 0.1 % Na Azide in 0.1 M phosphate buffer solution.

Histological Evaluation of 6-OHDA Lesion and Stereotactic Targeting

Coronal slices were rinsed in 0.01 M Phosphate buffered saline (PBS) with 0.2% Triton X-100 (PBS-Tx) and blocked in 10% normal goat serum in PBS-Tx for one hour before incubating with the primary antibody, anti-Tyrosine Hydroxylase (rabbit polyclonal, Abcam 1:4000), suspended in 10% normal goat serum (NGS) overnight at 4°C on a shaker. Each rinse was performed for two minutes and repeated three times. Following primary

incubation, sections were given three successive two-minute rinses in PBS-Tx. Slices were then incubated in 10% NGS for two hours at room temperature with the secondary antibody, goat anti-rabbit IgG conjugated to the fluorophore Alexa Fluor 647 (Thermo Fisher Scientific 1:200). Slides were then prepared to assess GRIN lens and STN lead placement. GRIN lens placement was visually confirmed to be within the dorsal striatum, a large and easily identifiable target, while STN lead placement was confirmed by overlaying of a mouse atlas[74] on images of each slice showing the tip of the STN stimulation electrode. Animals were excluded from analysis if neither of the two stimulating electrode contacts were located within the STN as assessed through histological analysis. Following secondary incubation, sections were given three successive two-minute rinses with 0.1M phosphate buffer, mounted onto subbed glass slides, and the coverslip was placed with ProLong Antifade Reagent containing DAPI (Thermo Fischer Scientific). Coronal slices were imaged using the Nikon Eclipse Ti microscope with Lumencor LED light source and Nikon Elements software. For assessment of the 6-OHDA lesion, tyrosine hydroxylase (TH) expression was quantified[75]. Images were obtained with a Tx Red filter cube and a shutter speed of 4ms at 50% LED power. Thresholds were set to (30-255) after performing rolling ball background subtraction with a 50 pixel radius using ImageJ (National Institutes of Health, Bethesda, MD). TH positive cell bodies in the substantia nigra were manually counted as described in Winkler et al.[76] and Santiago et al.[77]. In the dorsal striatum, mean-pixel intensity of the TH signal was quantified using ImageJ[78] as the sum of pixel values (0-255)/number of square pixels. Striatal regions deformed by the GRIN lens tract as observed in the histology were not included in the analysis of mean-pixel intensity.

Results and Discussion

This proof-of-principle study establishes a methodological framework for overcoming experimental and data analysis challenges associated with combining electrical stimulation with calcium imaging in freely moving animals. This was accomplished by demonstrating the use of calcium imaging via a head-mounted miniature fluorescence microscope to characterize the effects of electrical stimulation of the STN in awake-behaving parkinsonian mice. The experimental protocol consisted of AAV9 injections to induce GCaMP6m expression (Figure 2A), combined with placement of a GRIN lenses (Figure 2B), 6-OHDA lesioning (Figure 2A), and placement of bipolar stimulating electrodes (Figure 2B), validated separately in different animal cohorts.

Histological Validation of 6-OHDA Lesioning, GCaMP Expression, and Implant Positioning

The full experimental paradigm, consisting of 6-OHDA lesioning, AAV9 injection, GRIN lens implantation and STN stimulating electrode implantation, was performed on 10 mice after determining calcium imaging stability and the effects of stimulation in 6-OHDA lesioned mice. Two mice were lost due to surgical complications and two more due to GRIN lens damage that prevented imaging. An additional two mice were excluded from the analysis due to placement of the stimulating electrode outside of the STN.

In this paradigm, expression of GCaMP6m calcium indicator, induced by AAV9.CAG.GCaMP6m.WPRE.bGHpA injection, was confirmed via histological analysis that showed green fluorescent cell bodies in the dorsal striatum (Figure 3B). Dopaminergic lesioning via a unilateral 6-OHDA lesion, performed in the ipsilateral hemisphere, was confirmed by immunohistochemical labeling of TH followed by quantification of TH positive cells and mean pixel intensity (Figure 3A). A significant decrease in dorsal striatal mean pixel intensity (Figure 3D, $p < 0.05$; Welch's unequal variance t-test), and SNc TH positive cells (Figure 3E, $p < 0.05$; Welch's unequal variance t-test) between the lesioned and non-lesioned hemispheres was observed. Additionally, mice underwent GRIN lens implantation as well as implantation of a bipolar stimulation electrode consisting of a pair of 75 µm platinum wires in the STN (Figure 2B). These implant locations were confirmed
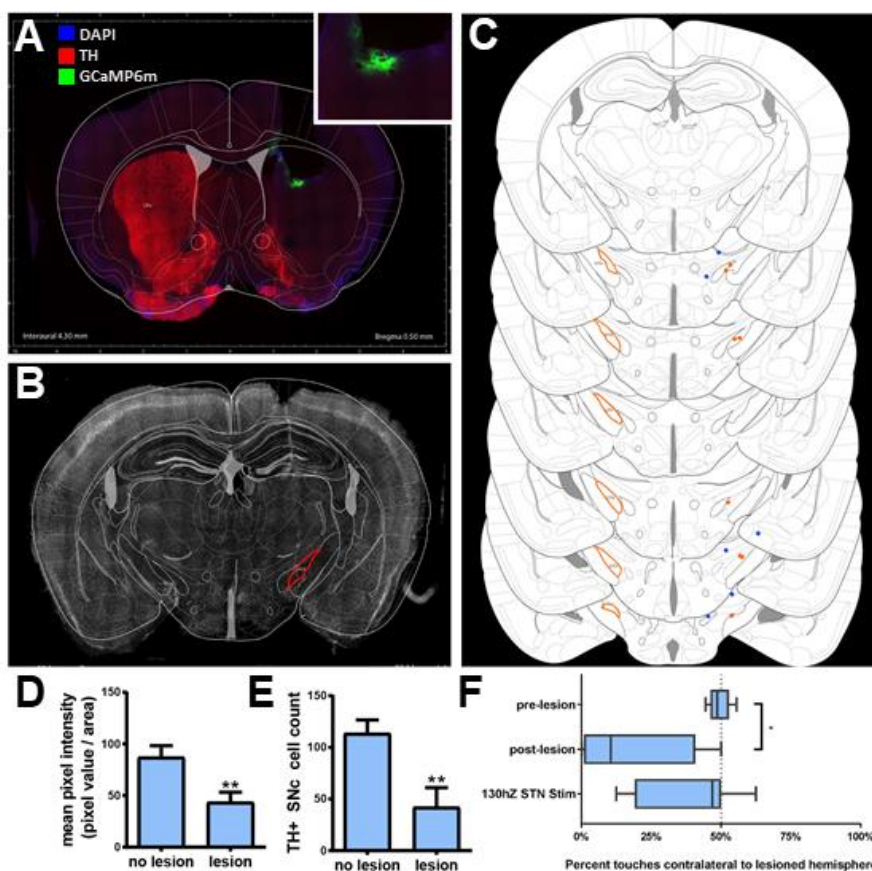
Figure 3. Histological and behavioral assessments. A) Coronal view of the histological analysis through the striatum showing lens placement, GCaMP6m expression (green label, inset), tyrosine hydroxylase (TH) stain (red label) demonstrating unilateral dopaminergic lesion in the striatum a healthy animal **B)** Coronal view indicating DBS electrode placement in the subthalamic nucleus (STN). **C)** A coronal atlas view showing DBS lead placement in 14 animals (orange dots indicate electrodes located within the STN, blue dots indicate electrodes placed outside of the STN) compared to the location of the STN outlined in orange on the contralateral hemisphere. **D)** TH+ mean pixel intensity (0-255) calculated over dorsal striatum, (Welch's unequal variance t-test, p<.05, n=10 F) and **E)** quantification of TH positive SNc cells in lesioned and non-lesioned hemispheres (Welch's unequal variance t-test p<.05, n=12; 1866 total cells), indicating successful 6-OHDA lesioning. **F)** Percentage contralateral paw touches pre and post 6-OHDA lesion and with 130Hz STN stimulation (p<0.005, Data represented as median, lower/upper quartiles and extremities, repeated measures one-way ANOVA with post-hoc Tukey's test), indicating greater limb-use asymmetry in 6-OHDA lesioned animals.

histologically via identification of a hypointense artifact located within the striatum and STN, respectively (Figure 3A,B). All lens implants were located within the dorsal striatum, while eight of fourteen stimulation electrodes were located within the STN (Figure 3C).

The complex nature of these experiments led to successful imaging in 40% of the animals, with primary failure points being anesthesia related complications during surgery (20%), lens damage during group housing of the animals (20%), and failure to place the STN stimulation electrode within the target structure (20%). Lens damage has since been mitigated in this experimental paradigm by covering the exposed lens with a protective cap fixed to the headcap with dental cement, which replaced the Kwik-Cast adhesive previously used.

10

Evaluation of Limb Use Asymmetry with and without Electrical Stimulation in a Parkinsonian Model

A cohort of 15 mice underwent 6-OHDA lesioning, implant of a mock GRIN lens (a glass rod of the same dimensions), and implant of a stimulating electrode into the STN. Of these, 8 animals were removed from the study due to failure of the stimulating electrode assessed by electrical impedance spectroscopy and using an impedance value greater than 120 kΩ at 130Hz as a cutoff between failed and working electrodes. A cylinder test, which is a commonly used method for assessing limb-use asymmetry in 6-OHDA lesioned animals[70–72], showed a significant decrease in the proportion of contralateral to ipsilateral paw touches as a result of 6-OHDA lesioning (Figure 3F, p<0.005; repeated measures one-way anova with post-hoc tukey test). A non-significant increase in the proportion of contralateral to ipsilateral paw touches was observed in mice electrically stimulated in the ipsilateral STN (Figure 3F, p=0.053; repeated measures one-way anova with post-hoc tukey test). Although a common clinical target for DBS, the effect of STN electrical stimulation on parkinsonian behavior in a mouse model has not been explored in previous studies. This study failed to observe a behavioral change associated with STN stimulation; however, the single behavioral test performed and unanticipated removal of animals, may have led to insufficient statistical power for evaluating this outcome. Additionally, the electrode configuration and parameters that best mimic the clinical DBS in mouse animal models are not well understood[79,80]. As such, a full validation of STN DBS in a parkinsonian
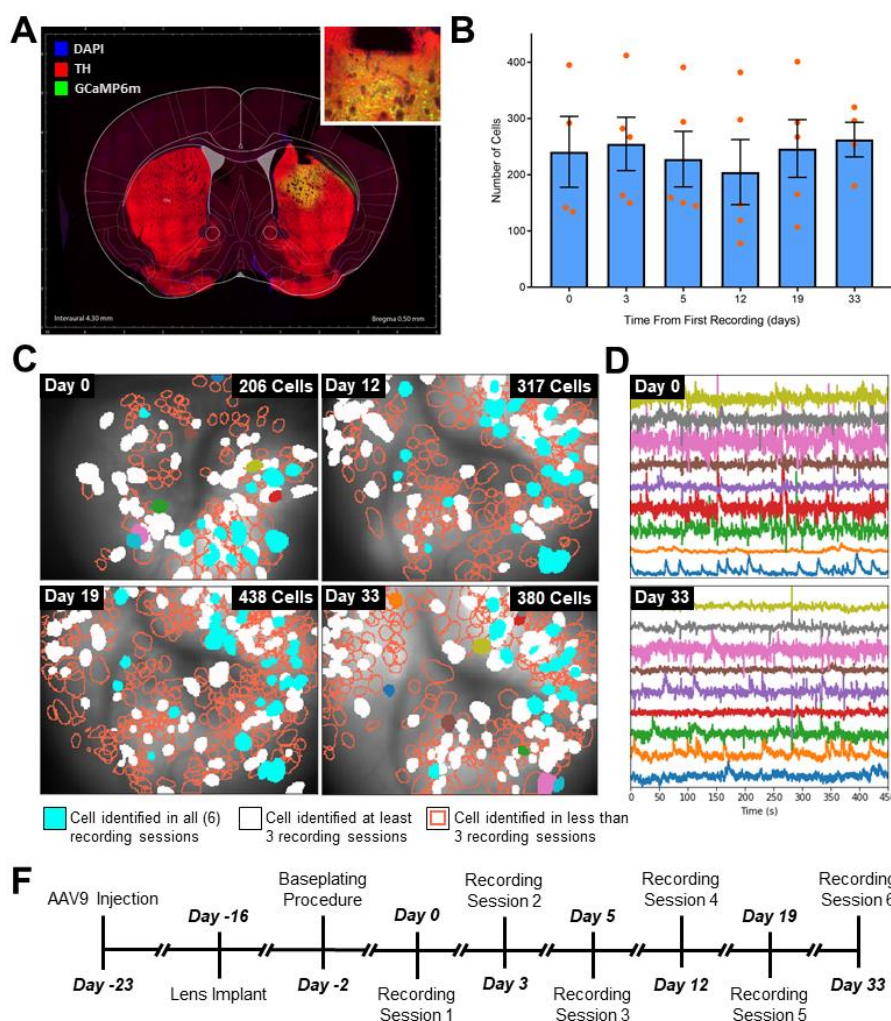

Figure 4. Chronic calcium recordings in healthy mice. A) A coronal view through the striatum of a healthy mouse indicating lens placement, GCaMP6m expression (green, inset), but no dopaminergic lesion as shown by the TH+ stain (red) for dopaminergic cells. **B)** The number of cells recorded across a cohort of five mice and identified using PCA/ICA was consistent over 33 days (p=0.89; one-way ANOVA). **C)** Representative mouse showing that the number of striatal neurons identified by CNMF-E was consistent over the course of the study. The different view on day 0 was the result of a microscope problem that required switching microscopes between Day 0 and 12. Light blue cells indicate cells that appeared in all six data sets recoded over 33 days, while cells displayed in white appeared in three or more data sets. **D)** Neural signals extracted from 10 cells appearing in all six recording sessions. These cells were selected at random. **F)** Experimental timeline for these experiments showing differences from the complete experimental protocol described in Figure 2.

mouse model that explores electrode configuration and stimulation parameters and utilizes a more complete repertoire of behavioral tests should be assessed in future experiments.

Another important consideration that needs to be further validated is the effect of tissue aspiration and GRIN lens implantation on the mechanisms underlying the effects of neuromodulation therapies[81]. For example, this procedure disrupts tissue within the motor cortex, striatum, and other structures which may be critical to the therapeutic effects of DBS. For this reason, it is paramount to understand the effect of the GRIN lens implant on both normal and pathological behaviors and response to therapeutic interventions. These questions will need to be addressed in detail by future studies using calcium imaging to study neuromodulation.

Chronic Calcium Imaging

Initial validation of calcium imaging within the striatum was performed in four mice from a cohort of five animals (Table 1); one mouse was lost due to surgical complications. Histological analyses showing green fluorescent cell bodies confirmed GCaMP expression and lens placement within the dorsal striatum (Figure 4A). Initially PCA/ICA, a commonly used analysis technique for calcium imaging data, was applied to identify cell activity but showed high correlation between calcium among nearby cells and was not able to distinguish overlapping cells bodies (Figure S2), a limitation that have been observed by other recent studies[59,82]. However, a consistent number of cells were obtained in recording sessions performed over 33 days (Figure 4B). To address the limitation of PCA/ICA, CNMF-E, currently a state-of-the-art analysis technique for head-mounted miniature microscope recordings, was applied for identification of neural signals and to assess the capabilities of single photon calcium imaging via a head-mounted microscope to obtain stable recordings over time. Analysis was performed to determine how many cells could be reliably tracked across multiple recording sessions, which is critical for enabling the study of long-term effects of neuromodulation therapies on neural activity (Figure 4C-D). Tracking of cells was performed using an algorithm based on the cell centroid locations and correlation of cell shapes described in Sheintuch et al. 2018[67], and showed cells appearing in all six recording sessions as well as a larger number of cells appearing in 3 or more recording sessions (Figure 4C).

Other studies using single and two photon microscopy in behaving animals have also shown stable longitudinal recordings in excess of one month[51,83–85]. These data suggest that longitudinal recording from the same cell population over weeks of neuromodulation therapy may be possible. Neuromodulation therapies for some neurologic and psychiatric conditions, such as depression and epilepsy can take months to show therapeutic effect[21,42–50]. The capability to longitudinally record from the same set of cells via calcium imaging in a deep brain region over weeks to months is important to enable the *in vivo* study of plasticity in neuromodulation therapies that can be difficult via electrophysiology or functional imaging methods.

Neural Signal Identification Techniques

To determine the effects of STN electrical stimulation on dorsal striatal activity, four anesthetized 6-OHDA lesioned mice were imaged during 10 second epochs of 30, 80 and 130 Hz stimulation separated by one-minute intervals to eliminate the residual effects from previous stimulations. This sequence was repeated 3 times in each animal. In this paradigm, which was selected to demonstrate the frequency-dependent effects of STN electrical stimulation, the striatum was quiescent while stimulation was turned off (Figure 5A) and only became active when STN stimulation was applied (Figure 5B-D). STN stimulation activated a subset of in-focus cells within the striatum
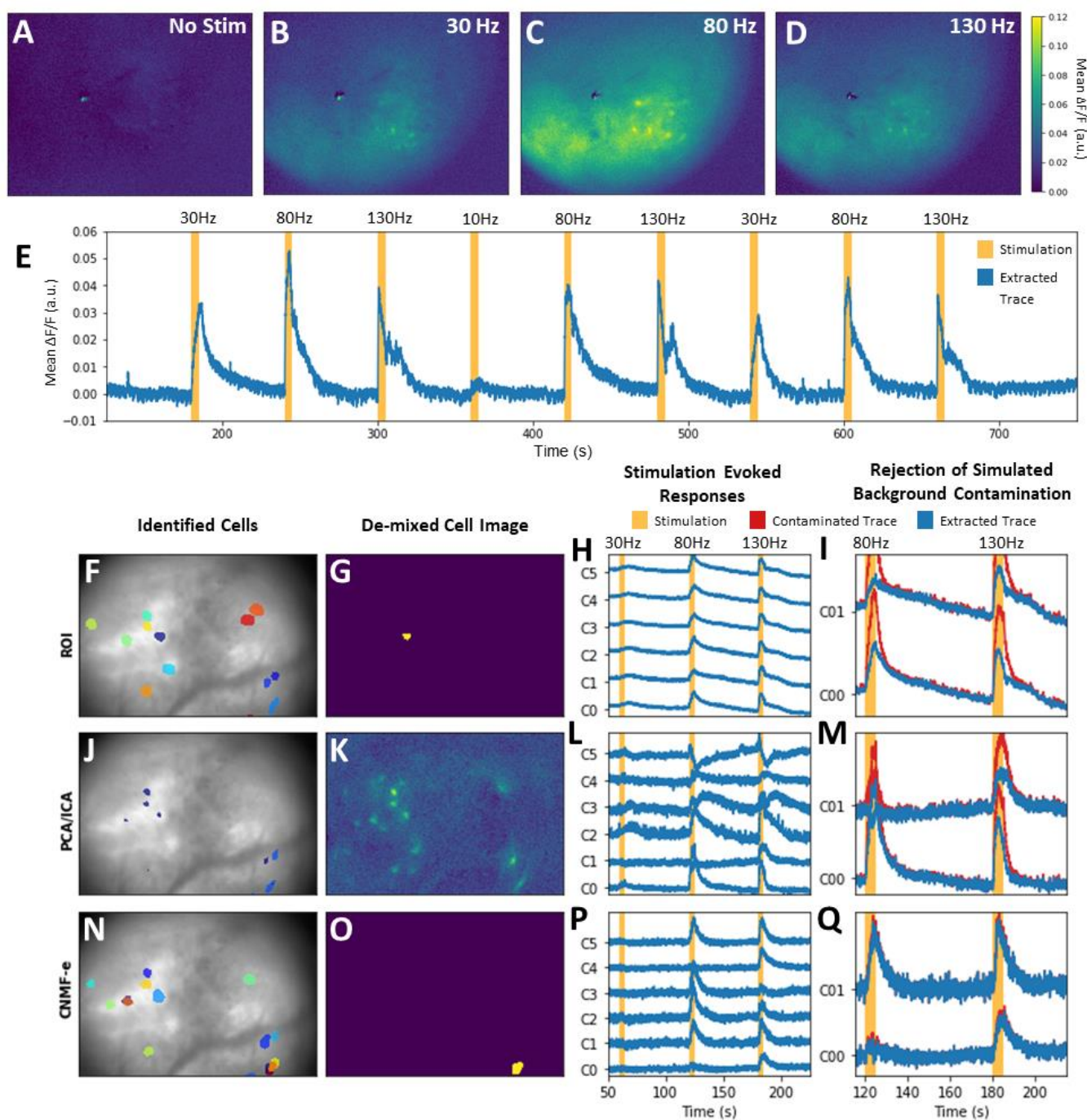
Figure 5. Data extraction techniques. A-D) Representative calcium responses evoked by different stimualation frequencies (no stimulation (A), 30 Hz (B), 80 Hz (C), and 130Hz (D) stimulation) in an anesthetized 6-OHDA lesioned mouse. **E)** The mean flourescence across the field of view during a sequence of stimulations shows large changes due to out-of-focus flourescence that is synchronized to the stimulation pulses applied. **F)** Individual cells identified by ROI analysis. **G)** A represetnative cell image obtained by ROI analysis showing a single well-defined cell body that was manually selected. **H)** Calcium traces during 30, 80, and 130 Hz stimulation trains that were extracted using ROI anaylsis. **I)** Calcium traces extracted using ROI analysis during two stimulations, plotted on top of extracted traces from the same dataset but contaminated with simulated background flourescence data. **J-M)** Similar data shown in panels **F-I** but extracted with PCA/ICA and exhibiting a failure to uniquely identify cell bodies (**K**). **N-Q)** The same data shown in panels **F-I** but extracted with CMMF-E to show the capabilities of CNMF-E to both uniquely identify cell bodies (**O**) as well as eliminate artificial background contamination from the identified cell-bodies (**Q**). These analysis were completed to determine which algorithms are well suited for identfying calcium activity in the presence of stimulation induced background contamination.

stimulation-evoked broad changes in cell activation. These stimulation-dependent out-of-focus signals are exemplified by changes in mean fluorescence within the field-of-view shown in Figure 5E. These out-of-focus changes and synchronous activation of multiple neurons confounded the analysis of calcium signals via standard data analysis techniques such as PCA/ICA, which identify cells using differences in temporal characteristics (Figure 5J-M). In order to select a suitable algorithm for identifying cells in data sets recorded during stimulation, simulated changes in background fluorescence based on a model of out-of-plane activation were added to an experimental data set (Fig. S2). To select the algorithm, the capability of three common data analysis methods and spatial filtering techniques to identify spatially compact neurons and remove the simulated contamination were compared.

ROI analysis, PCA/ICA with or without spatiotemporal de-mixing, and CNMF-e[59,60] were evaluated for their ability to extract well-defined cell bodies in the presence of real and simulated background fluorescence. Although ROI analysis allows for selection of well-defined cell bodies, it is a subjective technique and cannot separate cell activity from low spatial frequency background contamination. As a result, calcium traces extracted during electrical stimulation of the STN were nearly identical for all cells in the field of view (Figure 5H). This suggests that the traces were primarily the results of background contamination and not from individual neural activity. Additionally, ROI analysis was not able to remove simulated background contamination (Figure 5I). These results suggest that ROI analysis is not well suited for neuron identification from recordings obtained during electrical stimulation. Similar to ROI analysis, PCA/ICA[58] failed at uniquely identifying cells that exhibited synchronous firing during stimulation (Figure 5J-K) and was unable to completely remove artificial background contamination (Figure 5M). Spatiotemporal de-mixing, which can be used to improve the identification of cells with PCA/ICA[58], did not result in significant improvements (Figure S3A). Both ROI analysis and PCA/ICA were applied to the same data prefiltered using a spatial bandpass filter with cutoff frequencies chosen based on the size of cell bodies observed in the ΔF/F video (5 and 31 pixels). In both cases spatial filtering improved the rejection of artificial background contamination but did not completely eliminate the background contamination (Figure S3B-E).   In contrast, CNMF-E was able to identify individual cell bodies despite synchronous neural activity (Figure 5N-Q), does so an objective manner, and is much less susceptible to low spatial frequency background noise (Figure 5Q).

Unlike two-photon microscopy which is robust to changes in activity outside of the focal plane, single photon microscopy can be easily contaminated by out-of-focus changes in neural activity. Although these changes in activity may not significantly impact the analysis of neural activity during some behavioral paradigms, they can have a significant effect when electrical stimulation is applied. Therefore, attention should be paid to application of existing analysis techniques to the study of neuromodulation paradigms, which may introduce non-physiological changes in neural activity.

Frequency Dependence of STN Electrical Stimulation

A series of proof-of-principle experiments were performed to demonstrate the use of single-photon calcium imaging to study the effects of neuromodulation therapies in anesthetized and behaving animals. Other studies have shown that electrical stimulation excites neural elements in a frequency dependent manner[86] and that therapeutic responses to neuromodulation are highly dependent on stimulation frequency[87]. For example, therapeutic efficacy for STN DBS is typically achieved with high frequency stimulation in the range of 120-180 Hz[88]. To test for frequency dependent effects, four anesthetized mice were stimulated at 30, 80, and 130 Hz. Although the striatum was observed to be quiescent under anesthesia (Figure 5A), clear calcium activity suggestive of neuronal activation occurred with onset of STN stimulation (Figure 5B-D). The population of neurons activated by stimulation during anesthesia was a small subset of the neurons identified during awake behaving recordings (Figure 6A-C). This
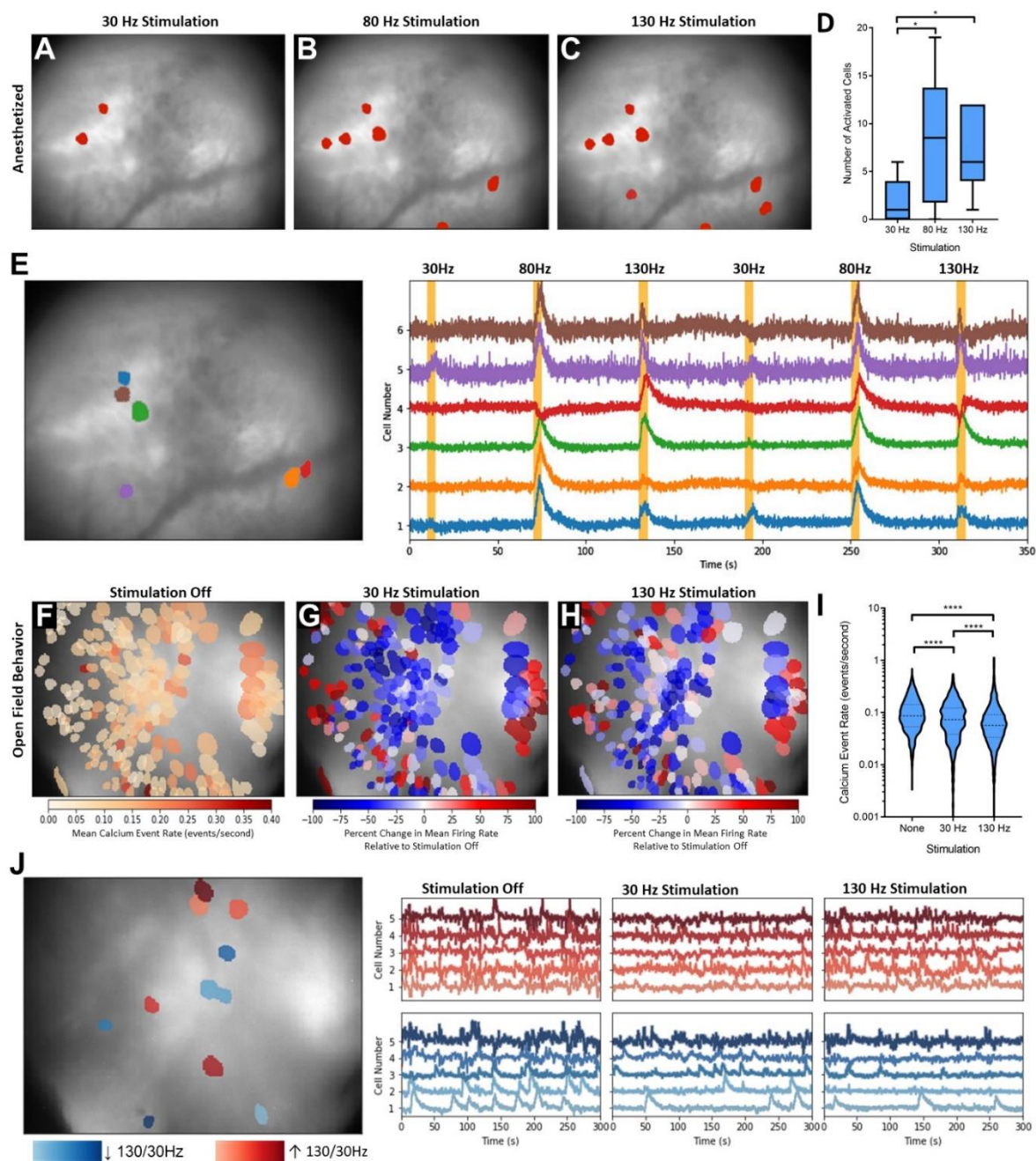
Figure 6. Frequency dependent responses to electrical stimulation of the subthalamic nucleus (STN). A-C) Cells responding to 30, 80, and 130 Hz stimulation, respectively, overlaid on the mean background image recorded in a representative anesthetized mouse. **D)** Mean number of activated cells responding to 30-130Hz stimulation in a cohort of four mice. Kruskal-Wallace one-way ANOVA, Dunn's multiple comparison test; * indicates p<0.05. **E)** Heterogeneity of neuronal responses to 30, 80, and 130Hz stimuli in one representative 6-OHDA lesioned mouse. **F)** Pseudocolored cells showing the mean firing rate of all identified cells in the field of view of one representative mouse over a ten - minute recording session in an open-field arena. **G-H)** Pseudocolored cells showing percent change in mean firing rate during 30 and 130 Hz stimulation, respectively. **I)** Mean calcium event rates observed in unstimulated as well as 30 and 130Hz stimulated mice during four recording sessions in two mice. Kruskal-Wallace one-way ANOVA, Dunn's multiple comparison test; **** indicates p<0.0001. **J)** Examples of cells showing the largest positive and negative differences in mean changes in firing rate in their response between 130 vs 30 Hz stimulation. Recordings during stimulation also exhibit a general decrease in activity compared the unstimulated recording session. These data show how optical imaging is well-suited for assessing the spatiotemporal changes in neural activity occurring during neuromodulation
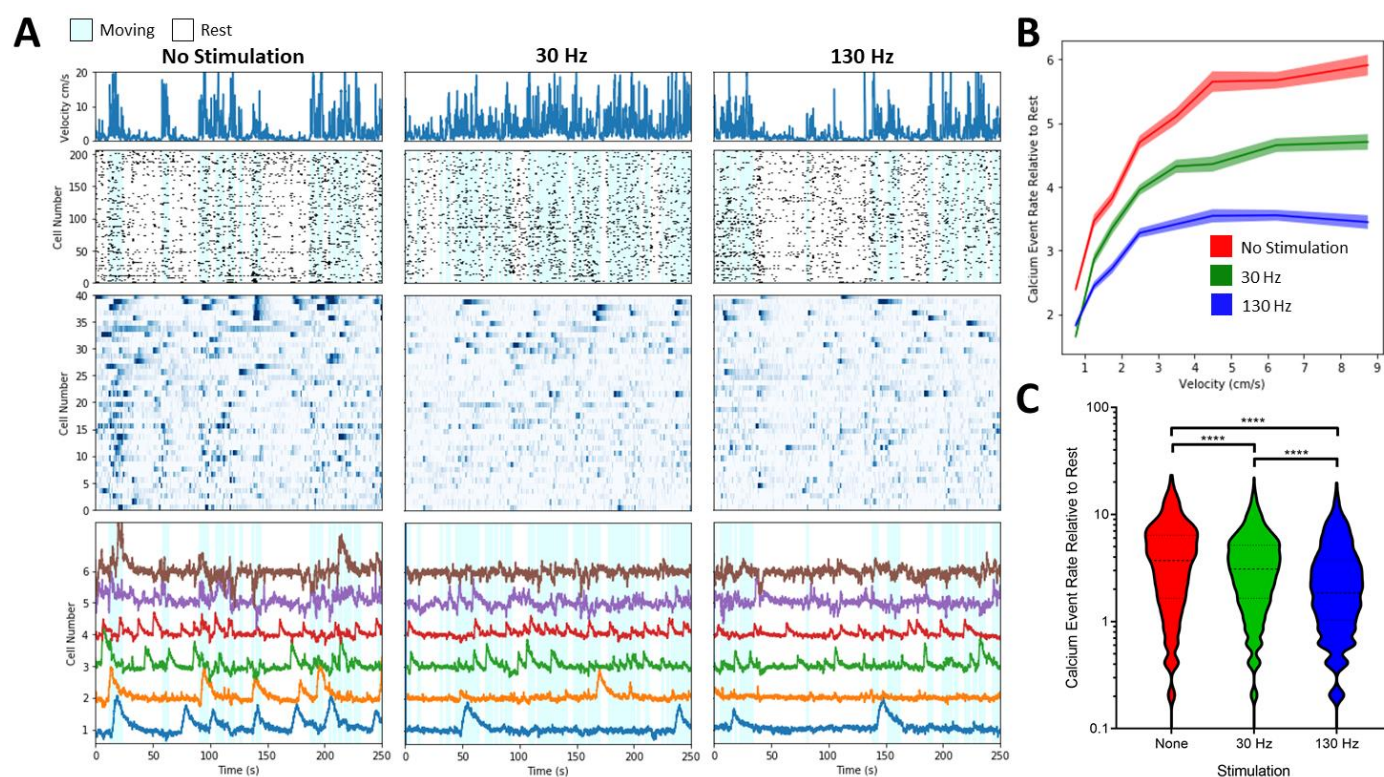
a
5

Figure 7. Relationship between neural activity and animal behavior (velocity) change with STN stimulation. A) Striatal cell activity (lower panels) was correlated with mouse behavior (top row), as measured by velocity, across stimulated and unstimulated open field behavior sessions. The second row displays the identified calcium events from all cells in a representative data set, while the third row represents calcium traces from 40 cells with the highest SNR in the same data set. The fourth row shows cell traces for the neurons with identified calcium events that are most correlated with mouse velocity during periods of no stimulation, showing examples increased activity during periods of movement. **B)** Differences in the relationship between the rate of calcium events normalized to no stimulation at rest (velocity < 0.5 cm/s) between all stimulation paradigms. This shows stimulation induced changes in the relationship between mouse behavior, assessed by velocity, and striatal activity. **C)** Significant differences in the relationship between the rate of calcium events normalized to no stimulation at rest (velocity < 0.5 cm/s) were observed between all stimulation paradigms. Kruskal-Wallace one-way analysis of variance, Dunn's multiple comparison test; **** indicates p<0.0001. These data suggest that calcium imaging in awake behaving animals can be used to assess the relationships between, neuromodulation therapies, pathological behavior in animal models of disease, and neural activity.

stimulation electrode[86,89]. Additionally, the recruitment occurred in a frequency-dependent manner (Fig. 6A-C) with 80 and 130 Hz stimulation exhibiting a greater number of activated cells than stimulation at 30Hz (Figure 6D, p<0.05; Kruskal-Wallace one-way analysis of variance, Dunn's multiple comparison test). Despite the frequency dependence of neural activation there was heterogeneity in the response of individual neurons to different stimulations as shown by Figure 6E. For instance, some cells only responded to stimulation at 80 Hz, but not 130Hz (i.e. Figure 6E, cell 2) or even showed heterogeneous responses to repeated stimulation at the same parameters (i.e. Figure 6E, cell 4), these cells did not necessarily depend on location of the cell in the field of view with co-localized neurons showing different responses to similar parameters (Figure 6E).

Two of these four mice also underwent awake-behaving imaging sessions in an open-field during stimulation (200µs pulsewidth, 30µA amplitude and 200µs pulsewidth, 80µA amplitude) following the anesthetized recordings. The striatal neural population was found to be highly active during open field behavior with increased

activity during animal movement (Figure 7A, Video S1). Additionally, neurons within the field of view exhibited heterogeneous firing rates shown in Figure 6F. Recordings during stimulation at both 30 Hz (Figure 6G) and 130 Hz (Figure 6H) showed a decrease in the activity of most striatal neurons in the field view (Figure I, p<0.0001 Kruskal-Wallace one-way analysis of variance, Dunn's multiple comparison test). In many cases, cells in striatum show increased activity during STN stimulation were spatially located next to cells evidencing a decrease in activity during stimulation. Additionally, subsets of cells showed both differences in their relative response to 130 vs. 30Hz stimulation (Figure 6J). Individual recording sessions were limited to 10 minutes in 6-OHDA lesioned mice, to prevent tangling of the microscope cord due to biased rotational behavior of the lesioned animals. In the future this recording time will be extended with the addition of a commutator[90–92].

In recordings obtained both under anesthesia and during open-field behavior, heterogeneous changes in neural activation occurred with stimulation. This heterogeneity may be due to differences in response of specific cell types or could be the result of subtle changes in stimulation evoked local neuronal/non-neuronal activity as a function of distance from the bipolar electrode leading to varied responses at a distal point in the connected circuit. Studies utilizing genetically indicators indictors with cell-types specific promotors or animal lines with cell-types specific indicator expression should be used in future studies to further parse out these effect on the neural circuits activated by neuromodulation therapies.

Stimulation Evoked Behavioral and Calcium Responses

Striatal cell activity was correlated with mouse behavior, as measured by velocity, across stimulated and unstimulated open field behavior sessions. This can be seen in the relationship between animal velocity (Figure 7A top row) and cell activity shown on the raster plots in Figure 7A rows 2 (identified calcium event timing for all cells in a representative data set) and 3 (calcium activity for the 40 highest SNR cells in the data set). Significant differences in the relationship between the rate of calcium events and animal velocity were observed at both 30 Hz Figure 7B,C; p<0.0001 Kruskal-Wallace one-way analysis of variance, Dunn's multiple comparison test) and 130 Hz (Figure 7B,C; p<0.0001 Kruskal-Wallace one-way analysis of variance, Dunn's multiple comparison test), suggesting that that the cellular effects of electrical stimulation of the STN may be dependent on the behavioral state of the animal. Head-mounted microscopy is uniquely suited for studying the relationship between changes in neural activity and behavior during therapeutic STN DBS. Additionally, the capability of calcium imaging techniques to record from genetically defined sub-populations of cells will allow for studying the effects of neuromodulation techniques in interesting neuronal cell-types, such as D1 and D2 medium spiny neurons that form the primary outputs of the striatum[51].

Conclusions

Optical imaging technologies such as single and two-photon imaging of calcium indicators as surrogates of neural activity have been widely adopted by neuroscientists for their ability to record from hundreds of single cells with cell-type specificity provided by genetically encoded indicators. These techniques are particularly well suited for studying the spatial dynamics in neural activity that orchestrate healthy behavior and the transition to maladaptive dynamics in a disease state[51]. Single photon microscopy via head-mounted microscopes has the distinct advantage of enabling calcium imaging in freely behaving animals and has already been utilized to show how cell-type specific spatial and temporal dynamics within the striatum break down in PD and are restored with pharmacological treatment[51]. Although this study describes preliminary data on the application of optical imaging, and specifically head-mounted miniature microscopy, for the study of electrical stimulation of the STN, these data

represent only one example of the myriad of applications for this technology in the study of the neuronal effects of neuromodulation.

References

1. Organization, W. H. *Neurological disorders. Public health challenges*. (World Health Organization, 2007).

2. Al-Harbi, K. S. Treatment-resistant depression: therapeutic trends, challenges, and future directions. *Patient Prefer. Adherence* **6**, 369–388 (2012).

3. Laxer, K. D. *et al.* The consequences of refractory epilepsy and its treatment. *Epilepsy Behav.* **37**, 59–70 (2014).

4. Benabid, A. L., Pollak, P., Louveau, A., Henry, S. & de Rougemont, J. Combined (thalamotomy and stimulation) stereotactic surgery of the VIM thalamic nucleus for bilateral Parkinson disease. *Appl. Neurophysiol.* **50**, 344–346 (1987).

5. Benabid, A. L. *et al.* Long-term suppression of tremor by chronic stimulation of the ventral intermediate thalamic nucleus. *The Lancet* **337**, 403–406 (1991).

6. Blomstedt, P. & Hariz, M. I. Deep brain stimulation for movement disorders before DBS for movement disorders. *Parkinsonism Relat. Disord.* **16**, 429–433 (2010).

7. Tröster, A. I., Meador, K. J., Irwin, C. P. & Fisher, R. S. Memory and mood outcomes after anterior thalamic stimulation for refractory partial epilepsy. *Seizure* **45**, 133–141 (2017).

8. Salanova, V. *et al.* Long-term efficacy and safety of thalamic stimulation for drug-resistant partial epilepsy. *Neurology* **84**, 1017–1025 (2015).

9. Fisher, R. *et al.* Electrical stimulation of the anterior nucleus of thalamus for treatment of refractory epilepsy. *Epilepsia* **51**, 899–908 (2010).

10. Thomas, G. P. & Jobst, B. C. Critical review of the responsive neurostimulator system for epilepsy. *Med. Devices Auckl. NZ* **8**, 405–411 (2015).

11. Parpura, V. *et al.* Neuromodulation: selected approaches and challenges. *J. Neurochem.* **124**, 436–453 (2013).

12. McIntyre, C. C. & Hahn, P. J. Network Perspectives on the Mechanisms of Deep Brain Stimulation. *Neurobiol. Dis.* **38**, 329–337 (2010).

13. Humphries, M. D. & Gurney, K. Network effects of subthalamic deep brain stimulation drive a unique mixture of responses in basal ganglia output. *Eur. J. Neurosci.* **36**, 2240–2251 (2012).

14. Miocinovic, S. *et al.* Computational Analysis of Subthalamic Nucleus and Lenticular Fasciculus Activation During Therapeutic Deep Brain Stimulation. *J. Neurophysiol.* **96**, 1569–1580 (2006).

15. Hashimoto, T., Elder, C. M., Okun, M. S., Patrick, S. K. & Vitek, J. L. Stimulation of the Subthalamic Nucleus Changes the Firing Pattern of Pallidal Neurons. *J. Neurosci.* **23**, 1916–1923 (2003).

16. Kita, H., Tachibana, Y., Nambu, A. & Chiken, S. Balance of Monosynaptic Excitatory and Disynaptic Inhibitory Responses of the Globus Pallidus Induced after Stimulation of the Subthalamic Nucleus in the Monkey. *J. Neurosci.* **25**, 8611–8619 (2005).

17. Smith, I. D. & Grace, A. A. Role of the subthalamic nucleus in the regulation of nigral dopamine neuron activity. *Synap. N. Y. N* **12**, 287–303 (1992).

18. Benazzouz, A. *et al.* Effect of high-frequency stimulation of the subthalamic nucleus on the neuronal activities of the substantia nigra pars reticulata and ventrolateral nucleus of the thalamus in the rat. *Neuroscience* **99**, 289–295 (2000).

19. Maurice, N., Thierry, A.-M., Glowinski, J. & Deniau, J.-M. Spontaneous and Evoked Activity of Substantia Nigra Pars Reticulata Neurons during High-Frequency Stimulation of the Subthalamic Nucleus. *J. Neurosci.* **23**, 9929–9936 (2003).

20. Malone, D. A. *et al.* Deep brain stimulation of the ventral capsule/ventral striatum for treatment-resistant depression. *Biol. Psychiatry* **65**, 267–275 (2009).

21. Mayberg, H. S. *et al.* Deep brain stimulation for treatment-resistant depression. *Neuron* **45**, 651–660 (2005).

22. Perlmutter, J. S. *et al.* Blood flow responses to deep brain stimulation of thalamus. *Neurology* **58**, 1388–1394 (2002).

23. Haslinger, B. *et al.* Differential modulation of subcortical target and cortex during deep brain stimulation. *NeuroImage* **18**, 517–524 (2003).

24. Deuschl, G. *et al.* The pathophysiology of parkinsonian tremor: a review. *J. Neurol.* **247 Suppl 5**, V33-48 (2000).

25. Schnitzler, A., Münks, C., Butz, M., Timmermann, L. & Gross, J. Synchronized brain network associated with essential tremor as revealed by magnetoencephalography. *Mov. Disord. Off. J. Mov. Disord. Soc.* **24**, 1629–1635 (2009).

26. Min, H.-K. *et al.* Subthalamic Nucleus Deep Brain Stimulation Induces Motor Network BOLD Activation: Use of a High Precision MRI Guided Stereotactic System for Nonhuman Primates. *Brain Stimulat.* **7**, 603–607 (2014).

27. Phillips, M. D. *et al.* Parkinson Disease: Pattern of Functional MR Imaging Activation during Deep Brain Stimulation of Subthalamic Nucleus—Initial Experience. *Radiology* **239**, 209–216 (2006).

28. Shon, Y.-M. *et al.* Effect of Chronic Deep Brain Stimulation of the Subthalamic Nucleus for Frontal Lobe Epilepsy: Subtraction SPECT Analysis. *Stereotact. Funct. Neurosurg.* **83**, 84–90 (2005).

29. Jonckers, E., Shah, D., Hamaide, J., Verhoye, M. & Van der Linden, A. The power of using functional fMRI on small rodents to study brain pharmacology and disease. *Front. Pharmacol.* **6**, (2015).

30. Lancelot, S. & Zimmer, L. Small-animal positron emission tomography as a tool for neuropharmacology. *Trends Pharmacol. Sci.* **31**, 411–417 (2010).

31. Lewis, C., Bosman, C. & Fries, P. Recording of brain activity across spatial scales. *Curr. Opin. Neurobiol.* **32**, 68–77 (2015).

32. Dickey, A. S., Suminski, A., Amit, Y. & Hatsopoulos, N. G. Single-Unit Stability Using Chronically Implanted Multielectrode Arrays. *J. Neurophysiol.* **102**, 1331–1339 (2009).

33. Tolias, A. S. *et al.* Recording chronically from the same neurons in awake, behaving primates. *J. Neurophysiol.* **98**, 3780–3790 (2007).

34. Parastarfeizabadi, M. & Kouzani, A. Z. Advances in closed-loop deep brain stimulation devices. *J. NeuroEngineering Rehabil.* **14**, (2017).

35. Nicolai, E. *et al.* Design Choices for Next-Generation Neurotechnology Can Impact Motion Artifact in Electrophysiological and Fast-Scan Cyclic Voltammetry Measurements. *Micromachines* **9**, 494 (2018).

36. Polikov, V. S., Tresco, P. A. & Reichert, W. M. Response of brain tissue to chronically implanted neural electrodes. *J. Neurosci. Methods* **148**, 1–18 (2005).

37. Butson, C. R., Maks, C. B. & McIntyre, C. C. Sources and effects of electrode impedance during deep brain stimulation. *Clin. Neurophysiol. Off. J. Int. Fed. Clin. Neurophysiol.* **117**, 447–454 (2006).

38. Fenoy, A. J., Goetz, L., Chabardès, S. & Xia, Y. Deep brain stimulation: are astrocytes a key driver behind the scene? *CNS Neurosci. Ther.* **20**, 191–201 (2014).

39. Ni, Z. *et al.* Pallidal deep brain stimulation modulates cortical excitability and plasticity. *Ann. Neurol.* **83**, 352–362 (2018).

40. So, R. Q., McConnell, G. C. & Grill, W. M. Frequency-dependent, transient effects of subthalamic nucleus deep brain stimulation on methamphetamine-induced circling and neuronal activity in the hemiparkinsonian rat. *Behav. Brain Res.* **320**, 119–127 (2017).

41. Giannicola, G. *et al.* The effects of levodopa and ongoing deep brain stimulation on subthalamic beta oscillations in Parkinson's disease. *Exp. Neurol.* **226**, 120–127 (2010).

42. Broadway, J. M. *et al.* Frontal Theta Cordance Predicts 6-Month Antidepressant Response to Subcallosal Cingulate Deep Brain Stimulation for Treatment-Resistant Depression: A Pilot Study. *Neuropsychopharmacology* **37**, 1764–1772 (2012).

43. Schulze-Bonhage, A. Brain stimulation as a neuromodulatory epilepsy therapy. *Seizure* **44**, 169–175 (2017).

44. Agnesi, F., Johnson, M. D. & Vitek, J. L. Deep brain stimulation: how does it work? *Handb. Clin. Neurol.* **116**, 39–54 (2013).

45. Temperli, P. *et al.* How do parkinsonian signs return after discontinuation of subthalamic DBS? *Neurology* **60**, 78–81 (2003).
46. Servello, D., Porta, M., Sassi, M., Brambilla, A. & Robertson, M. M. Deep brain stimulation in 18 patients with severe Gilles de la Tourette syndrome refractory to treatment: the surgery and stimulation. *J. Neurol. Neurosurg. Psychiatry* **79**, 136–142 (2008).
47. Sachdev, P. S. *et al.* Deep brain stimulation of the antero-medial globus pallidus interna for Tourette syndrome. *PloS One* **9**, e104926 (2014).
48. Greenberg, B. D. *et al.* Deep brain stimulation of the ventral internal capsule/ventral striatum for obsessive-compulsive disorder: worldwide experience. *Mol. Psychiatry* **15**, 64–79 (2010).
49. Tierney, T. S., Abd-El-Barr, M. M., Stanford, A. D., Foote, K. D. & Okun, M. S. Deep brain stimulation and ablation for obsessive compulsive disorder: evolution of contemporary indications, targets and techniques. *Int. J. Neurosci.* **124**, 394–402 (2014).
50. Dalkilic, E. B. Neurostimulation Devices Used in Treatment of Epilepsy. *Curr. Treat. Options Neurol.* **19**, 7 (2017).
51. Parker, J. G. *et al.* Diametric neural ensemble dynamics in parkinsonian and dyskinetic states. *Nature* **557**, 177–182 (2018).
52. Breese, G. R. & Traylor, T. D. Depletion of brain noradrenaline and dopamine by 6-hydroxydopamine. *Br. J. Pharmacol.* **42**, 88–99 (1971).
53. Barbera, G. *et al.* Spatially Compact Neural Clusters in the Dorsal Striatum Encode Locomotion Relevant Information. *Neuron* **92**, 202–213 (2016).
54. Klaus, A. *et al.* The Spatiotemporal Organization of the Striatum Encodes Action Space. *Neuron* **95**, 1171-1180.e7 (2017).
55. Resendez, S. L. *et al.* Visualization of cortical, subcortical and deep brain neural circuit dynamics during naturalistic mammalian behavior with head-mounted microscopes and chronically implanted lenses. *Nat. Protoc.* **11**, 566–597 (2016).
56. Kondo, T. *et al.* Calcium Transient Dynamics of Neural Ensembles in the Primary Motor Cortex of Naturally Behaving Monkeys. *Cell Rep.* **24**, 2191-2195.e4 (2018).
57. Thévenaz, P., Ruttimann, U. E. & Unser, M. A pyramid approach to subpixel registration based on intensity. *IEEE Trans. Image Process. Publ. IEEE Signal Process. Soc.* **7**, 27–41 (1998).
58. Mukamel, E. A., Nimmerjahn, A. & Schnitzer, M. J. Automated analysis of cellular signals from large-scale calcium imaging data. *Neuron* **63**, 747–760 (2009).
59. Zhou, P. *et al.* Efficient and accurate extraction of in vivo calcium signals from microendoscopic video data. *eLife* (2018). doi:10.7554/eLife.28728
60. Pnevmatikakis, E. A. *et al.* Simultaneous Denoising, Deconvolution, and Demixing of Calcium Imaging Data. *Neuron* **89**, 285–299 (2016).
61. Kerr, J. N. D., Greenberg, D. & Helmchen, F. Imaging input and output of neocortical networks in vivo. *Proc. Natl. Acad. Sci. U. S. A.* **102**, 14063–14068 (2005).
62. Dombeck, D. A., Khabbaz, A. N., Collman, F., Adelman, T. L. & Tank, D. W. Imaging large-scale neural activity with cellular resolution in awake, mobile mice. *Neuron* **56**, 43–57 (2007).
63. Ziv, Y. *et al.* Long-term dynamics of CA1 hippocampal place codes. *Nat. Neurosci.* **16**, 264–266 (2013).
64. Sun, C. *et al.* Distinct speed dependence of entorhinal island and ocean cells, including respective grid cells. *Proc. Natl. Acad. Sci.* **112**, 9466–9471 (2015).
65. Jennings, J. H. *et al.* Visualizing Hypothalamic Network Dynamics for Appetitive and Consummatory Behaviors. *Cell* **160**, 516–527 (2015).
66. Sivagnanam, S. *et al.* Introducing The Neuroscience Gateway. *CEUR Workshop Proc.* **993**, 7 (2013).
67. Sheintuch, L. *et al.* Tracking the Same Neurons across Multiple Days in Ca2+ Imaging Data. *Cell Rep.* **21**, 1102–1115 (2017).

68. Vogelstein, J. T. *et al.* Spike Inference from Calcium Imaging Using Sequential Monte Carlo Methods. *Biophys. J.* **97**, 636–655 (2009).

69. Jones, T. A. & Schallert, T. Use-dependent growth of pyramidal neurons after neocortical damage. *J. Neurosci. Off. J. Soc. Neurosci.* **14**, 2140–2152 (1994).

70. Glajch, K. E., Fleming, S. M., Surmeier, D. J. & Osten, P. Sensorimotor assessment of the unilateral 6-hydroxydopamine mouse model of Parkinson's disease. *Behav. Brain Res.* **230**, 309–316 (2012).

71. Lundblad, M., Picconi, B., Lindgren, H. & Cenci, M. A. A model of L-DOPA-induced dyskinesia in 6-hydroxydopamine lesioned mice: relation to motor and cellular parameters of nigrostriatal function. *Neurobiol. Dis.* **16**, 110–123 (2004).

72. Francardo, V. *et al.* Impact of the lesion procedure on the profiles of motor impairment and molecular responsiveness to L-DOPA in the 6-hydroxydopamine mouse model of Parkinson's disease. *Neurobiol. Dis.* **42**, 327–340 (2011).

73. Lempka, S. F., Miocinovic, S., Johnson, M. D., Vitek, J. L. & McIntyre, C. C. In vivo impedance spectroscopy of deep brain stimulation electrodes. *J. Neural Eng.* **6**, 046001 (2009).

74. Paxinos, G. & Franklin, K. B. J. *The Mouse Brain in Stereotaxic Coordinates*. (Gulf Professional Publishing, 2004).

75. Iancu, R., Mohapel, P., Brundin, P. & Paul, G. Behavioral characterization of a unilateral 6-OHDA-lesion model of Parkinson's disease in mice. *Behav. Brain Res.* **162**, 1–10 (2005).

76. Winkler, C., Kirik, D., Björklund, A. & Cenci, M. A. l-DOPA-Induced Dyskinesia in the Intrastriatal 6-Hydroxydopamine Model of Parkinson's Disease: Relation to Motor and Cellular Parameters of Nigrostriatal Function. *Neurobiol. Dis.* **10**, 165–186 (2002).

77. Santiago, R. M. *et al.* Depressive-like behaviors alterations induced by intranigral MPTP, 6-OHDA, LPS and rotenone models of Parkinson's disease are predominantly associated with serotonin and dopamine. *Prog. Neuropsychopharmacol. Biol. Psychiatry* **34**, 1104–1114 (2010).

78. Xavier, L. L. *et al.* A simple and fast densitometric method for the analysis of tyrosine hydroxylase immunoreactivity in the substantia nigra pars compacta and in the ventral tegmental area. *Brain Res. Brain Res. Protoc.* **16**, 58–64 (2005).

79. Gubellini, P., Salin, P., Kerkerian-Le Goff, L. & Baunez, C. Deep brain stimulation in neurological diseases and experimental models: From molecule to complex behavior. *Prog. Neurobiol.* **89**, 79–123 (2009).

80. Halpern, C. H., Attiah, M. A., Tekriwal, A. & Baltuch, G. H. A step-wise approach to deep brain stimulation in mice. *Acta Neurochir. (Wien)* **156**, 1515–1521 (2014).

81. Goss-Varley, M. *et al.* Microelectrode implantation in motor cortex causes fine motor deficit: Implications on potential considerations to Brain Computer Interfacing and Human Augmentation. *Sci. Rep.* **7**, 15254 (2017).

82. Lu, J. *et al.* MIN1PIPE: A Miniscope 1-Photon-Based Calcium Imaging Signal Extraction Pipeline. *Cell Rep.* **23**, 3673–3684 (2018).

83. Barretto, R. P. J. *et al.* Time-lapse imaging of disease progression in deep brain areas using fluorescence microendoscopy. *Nat. Med.* **17**, 223–228 (2011).

84. Ziv, Y. & Ghosh, K. K. Miniature microscopes for large-scale imaging of neuronal activity in freely behaving rodents. *Curr. Opin. Neurobiol.* **32**, 141–147 (2015).

85. Andermann, M. L. *et al.* Chronic Cellular Imaging of Entire Cortical Columns in Awake Mice Using Microprisms. *Neuron* **80**, 900–913 (2013).

86. Michelson, N. J., Islam, R., Vazquez, A. L., Ludwig, K. A. & Kozai, T. D. Y. Calcium activation of frequency dependent temporally phasic, localized, and dense population of cortical neurons by continuous electrical stimulation. (2018). doi:10.1101/338525

87. Dostrovsky, J. O. & Lozano, A. M. Mechanisms of deep brain stimulation. *Mov. Disord. Off. J. Mov. Disord. Soc.* **17 Suppl 3**, S63-68 (2002).

88. Grill, W. M., Snyder, A. N. & Miocinovic, S. Deep brain stimulation creates an informational lesion of the stimulated nucleus. *Neuroreport* **15**, 1137–1140 (2004).

89. Histed, M. H., Bonin, V. & Reid, R. C. Direct Activation of Sparse, Distributed Populations of Cortical Neurons by Electrical Microstimulation. *Neuron* **63**, 508–522 (2009).

90. Spieles-Engemann, A. L. *et al.* Stimulation of the rat subthalamic nucleus is neuroprotective following significant nigral dopamine neuron loss. *Neurobiol. Dis.* **39**, 105–115 (2010).

91. Li, X.-H. *et al.* High-frequency stimulation of the subthalamic nucleus restores neural and behavioral functions during reaction time task in a rat model of Parkinson's disease. *J. Neurosci. Res.* **88**, 1510–1521 (2010).

92. Liberti, W. A., Perkins, L. N., Leman, D. P. & Gardner, T. J. An open source, wireless capable miniature microscope system. *J. Neural Eng.* **14**, 045001 (2017).